Zitierweise: *Angew. Chem. Int. Ed.* **2024**, *63*, e202400313
doi.org/10.1002/anie.202400313

Self-Assembly

Diboraperylene Diborinic Acid Self-Assembly on Ag(111)—Kagome Flat Band Localized States Imaged by Scanning Tunneling Microscopy and Spectroscopy

Wun-Chang Pan, Carina Mützel, Soumyajyoti Haldar, Hendrik Hohmann, Stefan Heinze, Jeffrey M. Farrell, Ronny Thomale, Matthias Bode, Frank Würthner,* and Jing Qi**

Abstract: Replacement of sp^2-hybridized carbon in polycyclic aromatic hydrocarbons (PAHs) by boron affords electron-deficient π-scaffolds due to the vacant p_z-orbital of three-coordinate boron with the potential for pronounced electronic interactions with electron-rich metal surfaces. Using a diboraperylene diborinic acid derivative as precursor and a controlled on-surface non-covalent synthesis approach, we report on a self-assembled chiral supramolecular kagome network on an Ag(111) surface stabilized by intermolecular hydrogen-bonding interactions at low temperature. Scanning tunneling microscopy (STM) and spectroscopy (STS) reveal a flat band at ca. 0.33 eV above the Fermi level which is localized at the molecule center, in good agreement with tight-binding model calculations of flat bands characteristic for kagome lattices.

Introduction

During the last two decades, research on two-dimensional π-conjugated materials, being either connected by covalent bonds or by non-covalent interactions, enjoyed great popularity.[1,2] Whilst initially focused on purely carbon-based structures, more recent development also explored the influence of heteroatoms to tune the properties of the two-dimensional material and its coupling to substrate surfaces.[3] Substitutional doping with elements possessing more valence electrons than carbon, such as sulfur, phosphorus, selenium, oxygen, silicon, and nitrogen, affords electron-rich π-scaffolds that can be easily oxidized, thereby enabling *p*-type charge carrier transport.[4] Among them, nitrogen is the prevailing dopant, as it has a similar atomic radius to carbon.

The counterpart is boron, which only possesses three valence electrons, resulting in *n*-type organic semiconductors. Reports on boron-doped graphenes are, however, more scarce compared to those on nitrogen-doped graphenes.[5] To effectively tune the properties of boron-doped graphenes, the pattern and level of doping are crucial but unfortunately harder to control via the standard procedures (through chemical vapor deposition, solid-state and liquid-phase synthesis).[6] Therefore, cut-outs of boron-doped graphene, which are denoted as boron-containing graphene nanoribbons (GNRs), nanographenes, or polycyclic aromatic hydrocarbons (PAHs) depending on their size,[7–9] have attracted widespread interest as they can be accessed via bottom-up synthesis, allowing atom-precise structures.[7,10,11]

Starting with small precursors and making use of Au(111)-catalyzed coupling between brominated boron-containing PAH precursors, Kawai et al.[12] as well as Crommie and Fischer and co-workers[13] elegantly demonstrated in 2015 the synthesis of one-dimensional boron-doped graphene nanoribbons with defined structures. In this approach, strongly twisted precursor molecules are planarized on the substrate by covalent bond formation in a chemical reaction. An alternative approach to obtain boron-doped PAH layers

[*] W.-C. Pan, Prof. Dr. M. Bode, Dr. J. Qi
Experimentelle Physik 2, Physikalisches Institut, Julius-Maximilians-Universität Würzburg, Am Hubland, 97074 Würzburg, Germany
E-mail: jing.qi@uni-wuerzburg.de
Dr. C. Mützel, Prof. Dr. J. M. Farrell, Prof. Dr. F. Würthner
Institut für Organische Chemie, Julius-Maximilians-Universität Würzburg, Am Hubland, 97074 Würzburg, Germany
and
Center for Nanosystems Chemistry (CNC), Julius-Maximilians-Universität Würzburg, Theodor-Boveri-Weg, 97074 Würzburg, Germany
E-mail: wuerthner@uni-wuerzburg.de
Dr. S. Haldar, Prof. Dr. S. Heinze
Institut für Theoretische Physik und Astrophysik, Christian-Albrechts-Universität zu Kiel, 24098 Kiel, Germany
E-mail: haldar@physik.uni-kiel.de
H. Hohmann, Prof. Dr. R. Thomale
Institut für Theoretische Physik und Astrophysik, Julius-Maximilians-Universität Würzburg, Am Hubland, 97074 Würzburg, Germany
Prof. Dr. J. M. Farrell
Department of Chemistry, National Taiwan University, Roosevelt Road, 10617 Taipei, Taiwan

on metallic surfaces would rely on the self-assembly of suitable π-conjugated molecules.[2,14] Here, however, the common need for the stabilization of the reactive tricoordinate boron centers by sterically demanding substituents, such as mesityl, prohibits the formation of defined two-dimensional adlayers. Accordingly, despite of a large variety of boron-doped PAHs made available by the groups of Marder,[15] Yamaguchi,[16] Wagner,[17] Ingleson[18] and others,[19] such substituents protruding out of the π-plane interfere with the goal of self-assembly of such molecules in two-dimensional adlayers on planar surfaces. This problem also holds true for previously reported boron-containing PAHs from our group that typically are either helically twisted[20] or contain aromatic substituents that are twisted out of the boron-containing PAH plane.[21]

Here, following a previously introduced consecutive hydroboration/electrophilic borylation/dehydrogenation protocol,[22] we accomplished the first fully planar 3,9-diboraperylene diborinic acid derivative **B_2–Per** and demonstrate its suitability for the formation of well-organized self-assembled adlayers by vacuum-deposition on metallic surfaces. Using a low-temperature scanning tunneling microscope (LT-STM) and high-resolution bond-resolving imaging with carbon monoxide (CO) functionalized tips,[23] we reveal that **B_2–Per** on Ag(111) self-assembles by hydrogen bonds between the BOH subunits in a kagome lattice. Density functional theory (DFT) calculations indicate that this order relies on intermolecular bonds without any substrate atoms between the molecules. Tunneling spectroscopy reveals an empty state peak at an energy $eU \approx 330$ meV above the Fermi level which is located at the molecule center, in good agreement with tight-binding model calculations of flat bands characteristic for kagome lattices.[24]

Results and Discussion

3,9-Diboraperylene diborinic acid **B_2–Per** could be synthesized by the procedure shown in Scheme 1 that starts with the in situ generated borenium salt via a hydroboration/C–H borylation/dehydrogenation cascade followed by hydrolytic workup. For the details on the synthesis and compound characterization we refer to the experimental procedures section in Supporting Information.

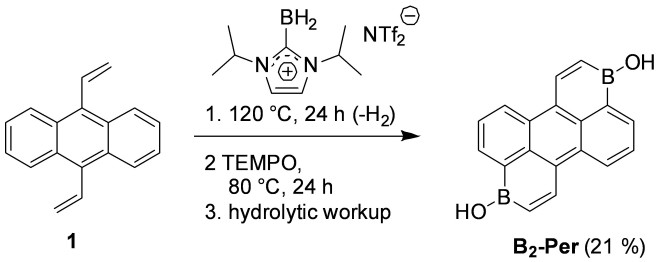

Scheme 1. One-pot synthesis of planar 3,9-diboraperylene diborinic acid **B_2–Per** from 9,10-divinylanthracene.

The optical properties of this molecule are indeed strikingly similar to those of perylene bisimides[25] (Figure 1); absorption and fluorescence maxima are almost at the same wavelengths for **B_2–Per** and perylene being functionalized with two imide substituents. Also, the vibronic patterns are very similar, which suggests a similar involvement of aromatic stretching vibrations and bond length variation upon excitation into the S_1 state for these two molecules. However, with a value of 69 % the fluorescence quantum yield (Φ_f) of **B_2–Per** in dichloromethane does not reach the same level as observed for many perylene bisimides (Φ_f close to 100 %). The redox potentials of −1.38 V and −1.80 V versus the ferrocenium/ferrocene redox couple determined for **B_2–Per** by cyclic voltammetry are also close to those observed for perylene bisimides (≈ −1.0 V and −1.2 V),[25,26] demonstrating the electron-accepting character induced by the two vacant p_z orbitals of the boron centers.

Prior to evaporation, **B_2–Per** was degassed for several hours under UHV conditions, and was afterwards sublimated from a resistively heated crucible onto a clean Ag(111) substrate kept at room temperature. The temperature of the crucible during evaporation is ~460 K. Clean Ag(111) surfaces were prepared by repeated cycles of Ar^+ ion sputtering for ~30 min at an ion energy of 1 keV and subsequent annealing up to 700 K for ~20 min.

After evaporation of the molecules, samples were immediately transferred into a home-built low-temperature scanning tunneling microscope (LT-STM) operated at $T \approx 4.5$ K. Topographic imaging was performed in the constant-current mode with the bias voltage applied to the sample. For scanning tunneling spectroscopy (STS) measurements, a bias voltage modulation U_{RMS} (frequency 1333.1 Hz) was applied such that tunneling differential conductance dI/dU spectra can be acquired by detecting the first harmonic signal with an external lock-in amplifier.

We first deposited **B_2–Per** on clean Ag(111) surfaces. The sample was annealed at 443 K for 20 min and then cooled down to 4.5 K in the STM. As shown in Figure 2a,

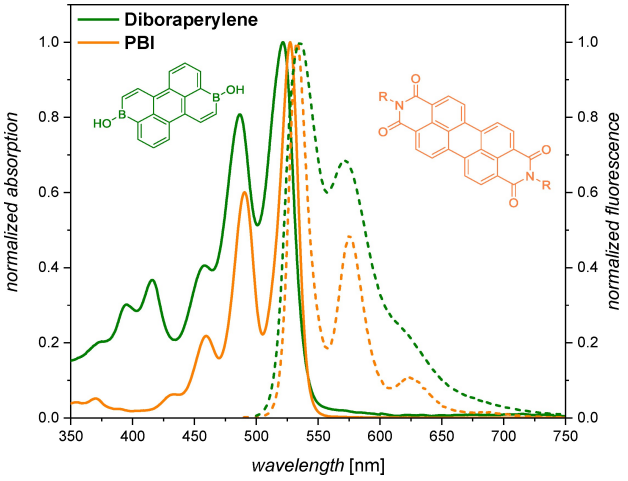

Figure 1. UV/Vis absorption and fluorescence spectra of **B_2–Per** in comparison to a perylene bisimide (R = *n*-hexyl) in dichloromethane at 298 K.

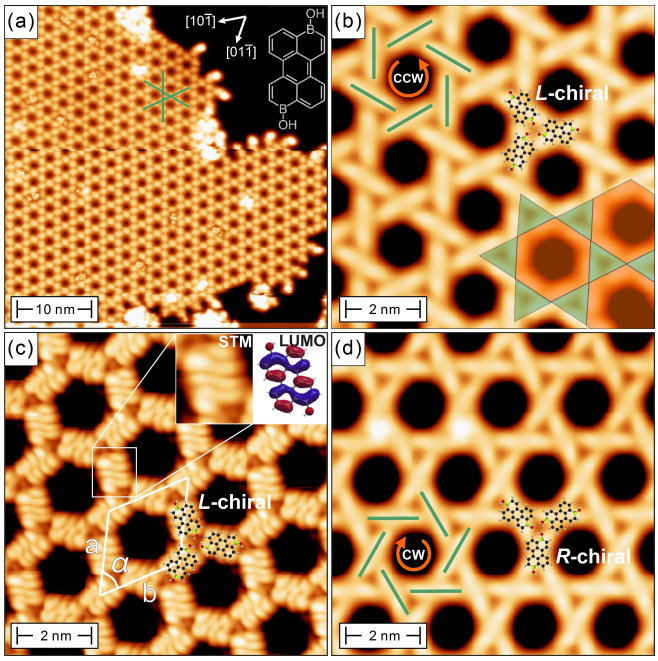

Figure 2. (a) STM topography of **B_2–Per** deposited on an Ag(111) surface and post-annealing at 443 K. The skeleton structure of the precursor (**B_2–Per**) is superimposed in the top right corner. (b,d) STM topographies of two typical kagome supramolecular structure areas under bias $U=-1$ V found on the same sample of (a), showing two opposite chiral rotations, i.e., counterclockwise (CCW) in (b) formed by ***L***-chiral molecules and clockwise (CW) in (d) formed by ***R***-chiral molecules. (c) Zoom-in image of (a) with a molecular functionalized tip shows the frontier molecular orbital of the kagome supramolecular network. Unit cell lengths and its included angle are marked as a, b and α. Molecular skeletons are superimposed for clarity. The inset shows the comparison of the STM topography and the DFT calculated lowest unoccupied molecular orbital (LUMO). Scanning parameters: (a) $U=1$ V, $I=100$ pA; (b) $U=-1$ V, $I=500$ pA; (c) $U=-100$ mV, $I=300$ pA; (d) $U=-1$ V, $I=800$ pA.

this preparation procedure led to extended islands of **B_2–Per**. A supramolecular network forms around hexagonally arranged holes. The edges of these islands are predominantly oriented along the three nearest-neighbor hole directions, indicated by green lines. Comparison with the atomic lattice of Ag(111) reveals that these directions are rotated by 14° with respect to the crystallographic $\langle 10\bar{1}\rangle$ directions of the substrate, indicated by white arrows in the upper right of Figure 2a.

Figure 2b shows a zoom-in STM image scanned at a bias voltage $U=-1$ V on an island similar to the one presented in Figure 2a. It becomes apparent that the symmetry of the molecular lattice exhibits a kagome lattice, as indicated by the colored p6 m-symmetric trihexagonal tiling pattern in the lower right of Figure 2b. Yet, similar to the structure of woven Japanese bamboo baskets which donated their name to the kagome lattice, mirror symmetry is broken at the vertices of the lattice, resulting in a chiral structure indicated by a pinwheel of green lines in the upper left of Figure 2b.

While this transition from a p6 m- to a p6-symmetric lattice in the case of bamboo baskets is a direct consequence of the weaving process, it is less straightforward to understand why the assembly of coplanar **B_2–Per** molecules on Ag(111) should result in a chiral surface structure. The origin of this chiral structure can be understood by a close inspection of high-resolution data obtained with a molecule-functionalized tip,[23,27] which is achieved by the accidental transfer of a **B_2–Per** molecule or clusters from the surface onto the tip apex. The data of Figure 2c were obtained on an island of **B_2–Per** similar to the one shown in Figure 2a and Figure 2b. The rhombus-shaped unit cell of the **B_2–Per** kagome lattice with the cell parameter $\vec{a}=(2.64\pm0.08)$ nm and an included angle $\alpha=(61\pm1)^\circ$ is clearly visible. We can also distinguish individual molecules. As expected for a kagome lattice, each molecule has four nearest neighbors, in contrast to the honeycomb, where each lattice site has three nearest neighbors.[24] Furthermore, the functionalized tip is able to reveal details of the molecule's orbital structure. The left inset of Figure 2c presents a zoom-in of a single **B_2–Per**. In the center one recognizes three, largely parallelly oriented features which exhibit an inverted s-shape. Two slightly elongated features can be found at the diagonally opposing molecule ends, i.e., in the upper right and the lower left of the left inset.

STM topographic images like the one presented in the left inset of Figure 2c, in simple terms, represent the local density of states (DOS) of the molecule over the range of biases from the electronic Fermi level to the set bias voltage. Therefore, it is meaningful to compare the experimental data to ab initio density functional theory (DFT) calculations. The right panel of the inset of Figure 2c shows the lowest unoccupied molecular orbital (LUMO) of a **B_2–Per** molecule (see details in Figure S8 in Supporting Information). The **B_2–Per** is prochiral, i.e., depending on the molecule's orientation upon landing on the substrate surface, either of the two molecular faces may point away from the substrate. We found that the experimental results of the inset of Figure 2c can only be reproduced for a left (***L***)-handed molecule, i.e., when the boron atoms are located at the upper left and lower right end of the molecule, resulting in enhanced charge density of the LUMO at the upper right and lower left end. Indeed, we recognize an excellent agreement between the experimental data and the DFT calculated LUMO.

The inspection of larger surface areas confirms that both islands with supramolecular networks consisting of ***L***- and ***R***-handed **B_2–Per** exist with the same probability. Exemplary STM images obtained at $U=-1$ V are presented in Figure 2b and d. In both panels, a pinwheel-like structure of lines can be recognized around the central depression. However, as indicated by green lines, the rotational sense of these pinwheel-like structures is opposite. While a counterclockwise (CCW) rotating pinwheel is found in Figure 2b, it is clockwise (CW) in Figure 2d. Note that the different handedness of these supramolecular networks also results in a rotation of the hexagonally arranged holes. While their nearest-neighbor direction is rotated by +14° in Figure 2b, like the island imaged in Figure 2a, the opposite rotation of −14° is observed for Figure 2d.

The data of Figure 2 lead to three major conclusions. (i) First, the good agreement between experimental data and DFT calculations confirms that the STM image represents the density of states of the **B_2–Per** LUMO. In the gas phase, this LUMO is found at an energy of 3.17 eV below the vacuum level, and 3.77 eV below the vacuum level if taken into account the intermolecular interactions (see details in section 3.1 in Supporting Information), which, given a Ag(111) work function of 4.53 eV,[28] would result in an energetical position far above the Fermi level. We speculate that the charge transfer between the substrate and the molecule results in a partial occupation of the LUMO. (ii) Second, it confirms the intactness of the molecule upon evaporation at ~460 K. (iii) Finally, it shows that islands of **B_2–Per** rotated by ±14° are formed by ***L***- and ***R***-chiral molecules, respectively. This can easily be understood by the prochirality of **B_2–Per** when adsorbed on two-dimensional surfaces.

To elucidate the interactions between **B_2–Per** molecules which lead to the kagome structure, we performed state-of-art bond-resolved STM (BR-STM) measurements[29] by utilizing carbon monoxide (CO) functionalized tips (see Supporting Information for details). It has been shown that Pauli repulsive forces caused by the tip-molecule interaction bend the CO molecule at the tip apex, resulting in sharp features which indicate intra- and inter-molecular chemical bonds in constant-height images.[30]

Figure 3a presents constant-height BR-STM data of one hexagonal **B_2–Per** ring area. To describe the observations, a scheme showing three molecules is added to the upper left. These symbols can be directly compared to the raw data presented in the circle. As symbolized by five hexagons, the three benzene rings and the two benzenoid rings where boron atoms are attached are clearly visible in the data, whereby the latter exhibit a larger charge density (brighter color). These rings are emphasized in the Fourier-filtered data shown in Figure 3b. Between the boron-doped benzenoid rings and the benzene ring of the neighboring **B_2–Per** a trapezoidal-shaped bridging structure with an enhanced charge density is observed. Furthermore, within the cavity formed by the three surrounding **B_2–Per** we frequently observe a discontinuous signal where the tunneling current abruptly changes (see black lines in the upper left of Figure 3a).

A contour map of the tunneling current measured in the constant-height mode is displayed in Figure 3c. The molecular skeletons of **B_2–Per** with an intramolecular B–C distance of ~0.72 nm (as calculated by DFT in the gas phase, see top left inset of Figure 3c, and in excellent agreement with the value of 0.718 nm observed in the crystal structure of a related previously reported derivative of **Br_2–Per**)[22] are superimposed to the BR-STM image for guidance of the eyes. This superposition results in a distance of the intramolecular benzenoid rings in STM data of (521.8 ± 9.4) pm, in good agreement with the theoretically expected value of 517.8 pm. This superposition allows us to sketch a potential binding configuration in the white box which is shown in detail in the inset in the lower left of Figure 3c. The measured distance between the boron-doped benzenoid

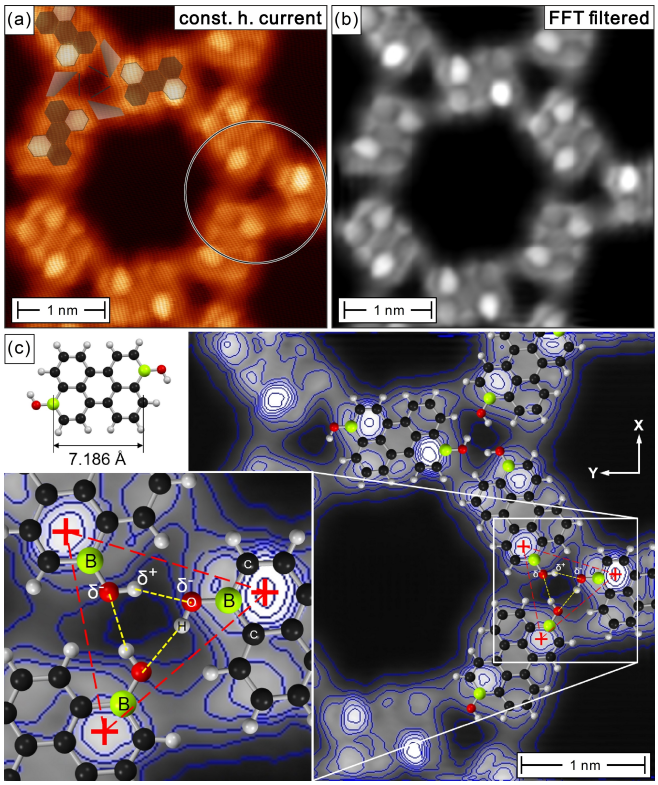

Figure 3. (a) Bond-resolved STM (BR-STM) constant-height image obtained with a CO-functionalized tip on one hexagonal molecular ring area. The grey and white hexagons indicate the fully carbon hexatomic ring and the carbon hexatomic ring with boron, respectively. The black lines indicate the feature where the tunneling current abruptly changes. The circle marks another ring area to be compared with that on the top left. The bias voltage was set to 2 mV during constant-height imaging. (b) Fourier-filtered images of (a). (c) Zoom-in of (b) with blue contour map at the top showing gradient apparent heights. Red crosses indicate the local maxima. Another zoom-in highlights the intermolecular area, where yellow dashed lines indicate the hydrogen bonds. The inset in the top left corner shows the B–C distance (~0.72 nm) of the DFT calculated **B_2–Per** molecule in the gas phase, which is used to scale the molecular skeletons superimposed on the STM image.

rings of two adjacent molecules (red crosses) amounts to (769.6 ± 15.7) pm. As indicated by yellow hatched lines, this would result in hydrogen bonds with a length of (220.5 ± 6.3) pm, in reasonable agreement with values reported in literature.[31]

The formation of kagome lattices via metal-organic networks has frequently been reported, which host a variety of correlated electronic phases, such as the Kondo effect[32] or superconductivity.[33] The question arises if the molecular network presented in Figures 2 and 3 is also held together by metal atoms, as reported by Kumar et al.[32] and Li et al.[34] Even though the **B_2–Per** molecules were deposited without any additional flux of evaporated metal, it is well-known that Ag atoms may detach from step edges at elevated temperatures and diffuse across the surface,[35–37] thereby providing a source of atoms which could be bound into the growing molecular network. Yet, on the basis of the results obtained by our BR-STM measurements (Figure 3)

and DFT-based STM simulations (see Figure S9–S12 in Supporting Information), we conclude that the **B_2–Per** kagome lattice on Ag(111) does not contain metal atoms. First, we never found any evidence for the existence of such atoms, as it was reported, for example, for the formation of para-hexaphenyl-dicarbonitrile and Cu on graphene.[34] Second, our DFT calculations show that the presence of an Ag atom in the shared triangular area increases the total energy up to several eV, depending on the specific binding sites (see Figure S9–S12 in Supporting Information). Therefore, we conclude that the kagome lattice is exclusively formed by hydrogen-bonded **B_2–Per** molecules.

After identifying the self-assembled supramolecular network of **B_2–Per** on Ag(111) as a p6-symmetric kagome lattice, the pertinent question arises if we find any evidence for flat bands which have been theoretically predicted and reported to exist.[24,38] Theoretical works have shown that the quantum-mechanical interference of electronic states in a kagome lattice with only nearest-neighbor hopping is completely destructive, resulting in "trapped particles"[39] with a vanishing energy dispersion, so-called flat bands. To answer this question, we performed scanning tunneling spectroscopy (STS) measurements by recording a differential conductance dI/dU spectrum at every of the 50 × 50 pixels of a 5 nm × 5 nm scan area, i.e., a spatial resolution of 100 pm (see video clip in Supporting Material). The real space representation reveals an enhanced DOS at the kagome sites (superimposed kagome lattice indicated in red) at an energy range of (+0.33 ± 0.05) eV, see Figure 4a. As shown in one exemplary dI/dU spectrum in Figure 4b, measured at the position of one kagome site in Figure 4a (red cross), this coincides with a prominent peak centered around +0.33 V. The enhanced DOS at the molecule center (the kagome site) is in agreement with the expected real space localization of flat bands in kagome systems.[24]

To substantiate this observation, we performed tight-binding model calculations of the E(k) band dispersion of a kagome lattice with hopping parameters t_1, t_2 and t_3, which represents the electronic hopping strength between each two nearest neighboring molecular sites in three orientations, as depicted in Figure 4a. Due to the three-fold symmetry shared by the intermolecular interaction area and the Ag(111) substrate, we assume equal hybridization strengths between the different nearest neighbors, i.e., $t_1 = t_2 = t_3 = t$. Diagonalizing the Hamiltonian yields three electronic bands: two dispersive bands featuring van Hove singularities (vHs) at the M-points while forming Dirac cones (DC) at the K-points, as well as a dispersionless flat band deriving from a destructive quantum interference imposed by the kagome structure. Among lattices with hexagonal point group symmetry the kagome lattice is special, and further exotic phenomena such as sublattice interference[40] are rooted in the kagome real space structure.

Having identified the flat band and attributing the dip in Figure 4b to the low density of states expected around the Dirac cone of the kagome model, we evaluate the hybridization strength to be $t \approx 0.44$ as well as the energy offset from pristine filling to be $\Delta E \approx -0.5466$. The dispersion E(k) is shown in Figure 4c. Deriving the DOS over the

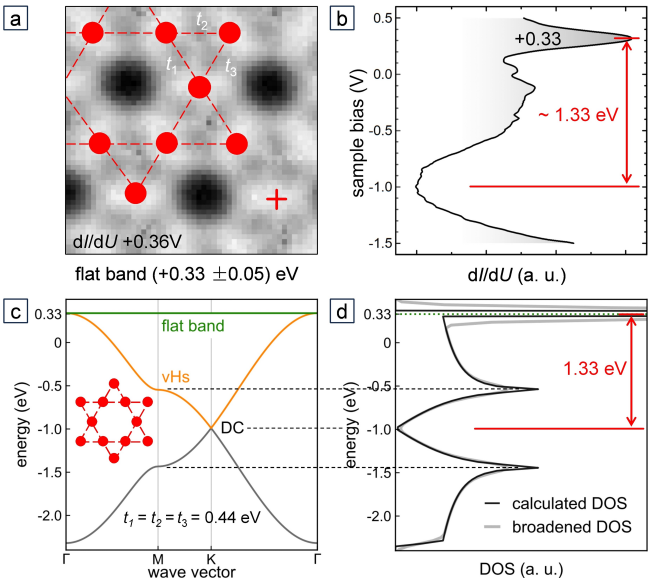

Figure 4. (a) The dI/dU map at +0.36 V shows localization features at the molecule centers. The superimposed kagome structure is indicated in red. t_1, t_2, and t_3 correspond to the hopping strength between three nearest neighbor molecular sites. (b) Differential conductance spectrum (dI/dU) measured at the center of the **B_2–Per** molecule (red cross in (a)). The energy gap between a flat band (+0.33 V) and the Dirac cone (−1.0 V) is ca. 1.33 eV. Stabilization parameter: U = 500 mV, I = 800 pA. (c) k-space dispersion of the electronic bands, i.e., E(k) diagram, calculated from a fitted tight-binding model with t_1, t_2 and t_3 set to 0.44 eV. (d) Calculated DOS from the E(k) diagram in (c), showing peaks at energies of the flat band and the van Hove singularities, as well as a dip at the Dirac cone.

energy scale, we recover the total DOS displayed in Figure 4d as a black curve, while a broadened DOS is displayed side-by-side as a grey curve, to be comparable with experimental DOS (see Supporting Information for details).

Comparing Figure 4b and Figure 4d, it becomes apparent that not only the position of the flat band and DC coincide but also the signature of the van Hove singularities can be roughly assigned to experimentally observed peak structures at around −0.57/−1.43 eV. Within subsequent studies, momentum-resolved measurement could unravel the distinct sublattice occupation at the three inequivalent van Hove points[40] within the supramolecular network. This would allow for a better understanding of the smeared upper van Hove peak while reinforcing the validity of our model. In conclusion, the agreement between experimentally measured dI/dU spectrum and the calculated DOS provides additional evidence that the localization feature in Figure 4a corresponds to the kagome flat band. Moreover, we propose an effective minimal model providing estimates for electronic characteristics of the supramolecular network such as electronic hopping strength and filling.

The presence of these site-specific electronic states strongly impacts the appearance of the self-assembled supramolecular network on Ag(111) in STM images (see video clip in Supporting Material for a complete data set, and Figure S14 in Supporting Information). This is evi-

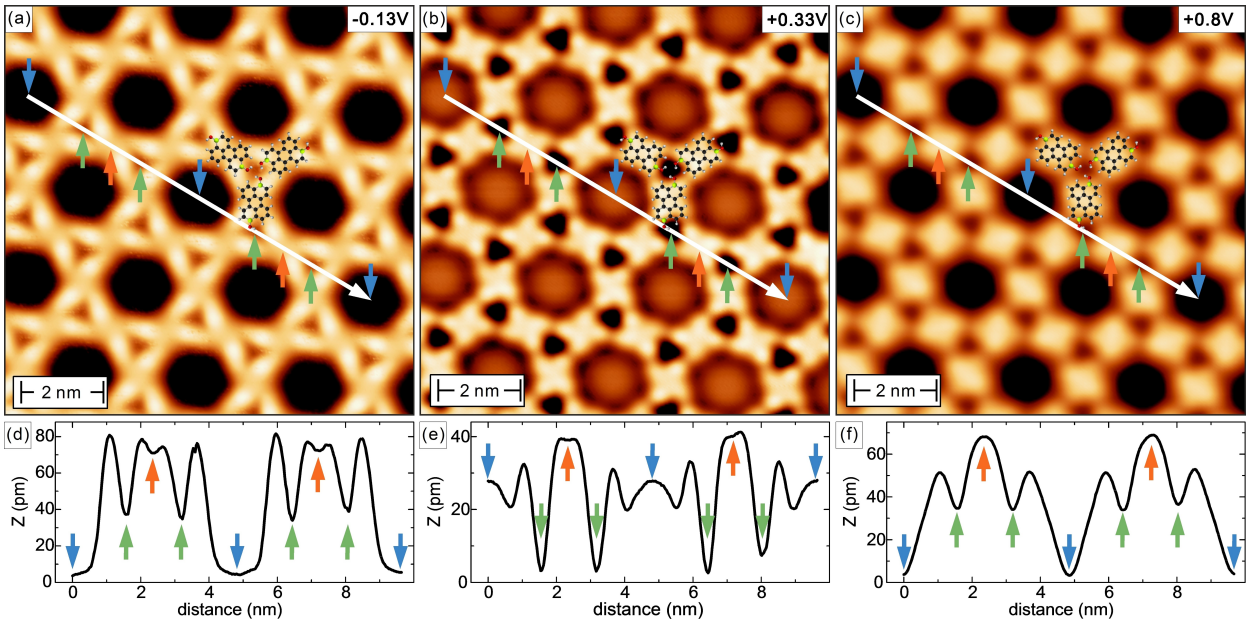

Figure 5. (a)-(c) Bias-dependent STM topographies of the same kagome supramolecular network. The molecular skeletons are superimposed. (d)-(f) Line sections drawn along the white arrows. Colored arrows highlight certain high-symmetry positions on the supramolecular network, i.e., substrate site (blue), honeycomb site (green), and kagome site (orange). Scanning parameters: (a)-(f) $I = 600$ pA; (a) $U = -330$ mV; (b) $U = 330$ mV; (c) $U = 800$ mV; (d) $U = -330$ mV; (e) $U = 330$ mV; (f) $U = 800$ mV.

denced by three topographic data sets recorded at bias voltages of $U = -0.13$ V, $+0.33$ V, and $+0.8$ V in Figure 5a–c, respectively. In Figure 5a the bonding orbitals located at the intermolecular bonds dominate. Therefore, the apparent height is maximal approximately at the location of the three bonds within the shared triangle area, as can be seen in the line section plotted in Figure 5d. At $U = +0.33$ V, we are close to the strong peak which appears at the shared triangle area. Correspondingly, the depth of the hole at the hexagonal sites is strongly reduced (see line section in Figure 5e). Finally, if the bias voltage is increased well beyond the peak and shoulder of the kagome site, a roughly square-shaped feature centered at the **B_2–Per** molecule can be recognized. We also recognize a contrast reversal of high and low DOS within the shared triangular area at different bias voltages in dI/dU maps (see Figure S13 in Supporting Information), which we attribute to the bonding- and antibonding-like orbital signatures in the intermolecular area.

Conclusion

In summary, we have reported the synthesis of a fully planar 3,9-diboraperylene derivative **B_2–Per** and its self-assembled supramolecular kagome network formed through on-surface non-covalent synthesis on Ag(111) surface under low temperature and vacuum conditions. The kagome supramolecular network of a chiral and 120° head-to-head assembly formed by the **B_2–Per** is evidenced to be stabilized by intermolecular interactions, i.e., hydrogen bonds, without any substrate adatom in between. A dispersionless flat band at ~0.33 eV above the Fermi level is observed in both tunneling spectroscopy and dI/dU maps, which is further proved by the tight-binding model calculations. Our work has broadened the knowledge of the fabrication of two-dimensional (2D) complex supramolecular networks on metal surfaces as well as their electronic properties, offering yet another template on which nontrivial topology can be tuned.

Acknowledgements

F.W. thanks the German Research Foundation (Deutsche Forschungsgemeinschaft, DFG) for financial support (WU 317/23-1). M.B., R.T., and J.Q. acknowledge financial support from DFG under Germany's Excellence Strategy through Würzburg-Dresden Cluster of Excellence on Complexity and Topology in Quantum Matter-ct.qmat (EXC 2147, Project-id 390858490). S.Ha. and S.He. thank the financial support from DFG via Project-id No. 418425860 and No. 445697818. S.Ha. and S.He. gratefully acknowledge computing time at the supercomputer of the North-German Supercomputing Alliance (HLRN). C.M. and F.W. thank Carolin Ottohal for her synthetic contributions to this project in her Bachelor's thesis. H.H. acknowledges stimulating discussions with T. Müller. J.Q. gratefully acknowledges valuable discussions with J. Qin, X. Cai, H. Fu, A. K. Swain, F. Zhang, V. Brancaccio, C. Li, F. Xiang, Q. Zhong, P. Jelínek and B. Liu. Open Access funding enabled and organized by Projekt DEAL.

Conflict of Interest

The authors declare no conflict of interest.

Data Availability Statement

The data that support the findings of this study are available from the corresponding author upon reasonable request.

Keywords: boron · polycycles · self-assembly · intermolecular interactions · scanning tunneling microscopy and spectroscopy

[1] R. H. Dong, T. Zhang, X. Feng, *Chem. Rev.* **2018**, *118*, 6189–6235.
[2] J. A. A. W. Elemans, S. B. Lei, S. De Feyter, *Angew. Chem. Int. Ed.* **2009**, *48*, 7298–7332; *Angew. Chem.* **2009**, *121*, 7434–7469.
[3] S. Agnoli, M. Favaro, *J. Mater. Chem. A* **2016**, *4*, 5002–5025.
[4] M. Stepien, E. Gonka, M. Zyla, N. Sprutta, *Chem. Rev.* **2017**, *117*, 3479–3716.
[5] H. X. Xu, L. B. Ma, Z. Jin, *J. Energy Chem.* **2018**, *27*, 146–160.
[6] Z. H. Sheng, H. L. Gao, W. J. Bao, F. B. Wang, X. H. Xia, *J. Mater. Chem. C* **2012**, *22*, 390–395.
[7] X. Xu, K. Müllen, A. Narita, *Bull. Chem. Soc. Jpn.* **2020**, *93*, 490–506.
[8] X. Feng, W. Pisula, K. Müllen, *Pure Appl. Chem.* **2009**, *81*, 2203–2224.
[9] W. Pisula, X. Feng, K. Müllen, *Adv. Mater.* **2010**, *22*, 3634–3649.
[10] S. Kawai, S. Nakatsuka, T. Hatakeyama, R. Pawlak, T. Meier, J. Tracey, E. Meyer, A. S. Foster, *Sci. Adv.* **2018**, *4*, eaar7181.
[11] M. Krieg, F. Reicherter, P. Haiss, M. Ströbele, K. Eichele, M.-J. Treanor, R. Schaub, H. F. Bettinger, *Angew. Chem. Int. Ed.* **2015**, *54*, 8284–8286; *Angew. Chem.* **2015**, *127*, 8402–8404.
[12] S. Kawai, S. Saito, S. Osumi, S. Yamaguchi, A. S. Foster, P. Spijker, E. Meyer, *Nat. Commun.* **2015**, *6*, 8098.
[13] R. R. Cloke, T. Marangoni, G. D. Nguyen, T. Joshi, D. J. Rizzo, C. Bronner, T. Cao, S. G. Louie, M. F. Crommie, F. R. Fischer, *J. Am. Chem. Soc.* **2015**, *137*, 8872–8875.
[14] J.-J. Zhang, J. Ma, X. Feng, *Macromol. Chem. Phys.* **2023**, *224*, 2200232.
[15] L. Ji, S. Griesbeck, T. B. Marder, *Chem. Sci.* **2017**, *8*, 846–863.
[16] a) C. Dou, S. Saito, K. Matsuo, I. Hisaki, S. Yamaguchi, *Angew. Chem. Int. Ed.* **2012**, *51*, 12206–12210; *Angew. Chem.* **2012**, *124*, 12372–12376; b) For a recently reported flat derivative, see: N. Ando, T. Yamada, H. Narita, N. N. Oehlmann, M. Wagner, S. Yamaguchi, *J. Am. Chem. Soc.* **2021**, *143*, 9944–9951.
[17] a) A. John, M. Bolte, H.-W. Lerner, M. Wagner, *Angew. Chem. Int. Ed.* **2017**, *56*, 5588–5592; *Angew. Chem.* **2017**, *129*, 5680–5684; b) V. M. Hertz, M. Bolte, H.-W. Lerner, M. Wagner, *Angew. Chem. Int. Ed.* **2015**, *54*, 8800–8804; *Angew. Chem.* **2015**, *127*, 8924–8928; c) J. Radtke, K. Schickedanz, M. Bamberg, L. Menduti, D. Schollmeyer, M. Bolte, H.-W. Lerner, M. Wagner, *Chem. Sci.* **2019**, *10*, 9017–9027.
[18] a) D. L. Crossley, R. J. Kahan, S. Endres, A. J. Warner, R. A. Smith, J. Cid, J. J. Dunsford, J. E. Jones, I. Vitorica-Yrezabal, M. J. Ingleson, *Chem. Sci.* **2017**, *8*, 7969–7977; b) K. Yuan, R. J. Kahan, C. Si, A. Williams, S. Kirschner, M. Uzelac, E. Zysman-Colman, M. J. Ingleson, *Chem. Sci.* **2020**, *11*, 3258–3267.
[19] a) J. Chen, J. W. Kampf, A. J. Ashe, *Organometallics* **2008**, *27*, 3639–3641; b) K. Hirano, K. Morimoto, S. Fujioka, K. Miyamoto, A. Muranaka, M. Uchiyama, *Angew. Chem. Int. Ed.* **2020**, *59*, 21448–21453; *Angew. Chem.* **2020**, *132*, 21632–21637; c) Y. Xia, M. Zhang, S. Ren, J. Song, J. Ye, M. G. Humphrey, C. Zheng, K. Wang, X. Zhang, *Org. Lett.* **2020**, *22*, 7942–7946; d) J.-J. Zhang, M.-C. Tang, Y. Fu, K.-. H. Low, J. Ma, L. Yang, J. J. Weigand, J. Liu, V. W.-W. Yam, X. Feng, *Angew. Chem. Int. Ed.* **2021**, *60*, 2833–2838; *Angew. Chem.* **2021**, *133*, 2869–2874:.
[20] C. Mützel, J. M. Farrell, K. Shoyama, F. Würthner, *Angew. Chem. Int. Ed.* **2022**, *61*, e202115746; *Angew. Chem.* **2022**, *61*, e202115746.
[21] J. M. Farrell, C. Mützel, D. Bialas, M. Rudolf, K. Menekse, A.-M. Krause, M. Stolte, F. Würthner, *J. Am. Chem. Soc.* **2019**, *141*, 9096–9104.
[22] J. M. Farrell, D. Schmidt, V. Grande, F. Würthner, *Angew. Chem. Int. Ed.* **2017**, *56*, 11846–11850; *Angew. Chem.* **2017**, *129*, 12008–12012.
[23] P. Hapala, G. Kichin, C. Wagner, F. S. Tautz, R. Temirov, P. Jelínek, *Phys. Rev. B* **2014**, *90*, 085421.
[24] C. Barreteau, F. Ducastelle, T. Mallah, *J. Phys. Condens. Matter* **2017**, *29*, 465302.
[25] A. Nowak-Król, K. Shoyama, M. Stolte, F. Würthner, *Chem. Commun.* **2018**, *54*, 13763–13772.
[26] R. Renner, M. Stolte, J. Heitmüller, T. Brixner, C. Lambert, F. Würthner, *Mater. Horiz.* **2022**, *9*, 350–359.
[27] L. Gross, *Nat. Chem.* **2011**, *3*, 273–278.
[28] G. N. Derry, M. E. Kern, E. H. Worth, *J. Vac. Sci. Technol. A* **2015**, *33*, 060801.
[29] D. G. de Oteyza, P. Gorman, Y.-C. Chen, S. Wickenburg, A. Riss, D. J. Mowbray, G. Etkin, Z. Pedramrazi, H.-Z. Tsai, A. Rubio, M. F. Crommie, F. R. Fischer, *Science* **2013**, *340*,1434–1437.
[30] P. Hapala, R. Temirov, F. S. Tautz, P. Jelínek, *Phys. Rev. Lett.* **2014**, *113*, 226101.
[31] a) A. Brinkmann, A. P. M. Kentgens, *J. Am. Chem. Soc.* **2006**, *128*, 46, 14758–14759; b) R. Taylor, O. Kennard, *Acc. Chem. Res.* **1984**, *17*, 320–326.
[32] D. Kumar, J. Hellerstedt, B. Field, B. Lowe, Y. Yin, N. V. Medhekar, A. Schiffrin, *Adv. Funct. Mater.* **2021**, *31*, 2106474.
[33] T. Takenaka, K. Ishihara, M. Roppongi, Y. Miao, Y. Mizukami, T. Makita, J. Tsurumi, S. Watanabe, J. Takeya, M. Yamashita, K. Torizuka, Y. Uwatoko, T. Sasaki, X. Huang, W. Xu, D. Zhu, N. Su, J.-G. Cheng, T. Shibauchi, K. Hashimoto, *Sci. Adv.* **2021**, *7*, eabf3996.
[34] J. Li, L. Solianyk, N. Schmidt, B. Baker, S. Gottardi, J. Carlos M Lopez, M. Enache, L. Monjas, R. van der Vlag, R. W. A. Havenith, A. K. H. Hirsch, M. Stöhr, *J. Phys. Chem. C* **2019**, *123*, 12730–12735.
[35] M. Giesen, G. Schulze, I. Konert, *Surf. Sci.* **1998**, *412/413*, 645–656.
[36] G. Rosenfeld, K. Morgenstern, M. Esser, G. Comsa, *Appl. Phys. A* **1999**, *69*, 489–496.
[37] N. Quaas, M. Wenderoth, R. G. Ulbrich, *Surf. Sci.* **2004**, *550*, 57–64.
[38] H.-M. Guo, M. Franz, *Phys. Rev. B* **2009**, *80*, 113102.
[39] Z. Li, J. Zhuang, L. Wang, H. Feng, Q. Gao, X. Xu, W. Hao, X. Wang, C. Zhang, K. Wu, S. X. Dou, L. Chen, Z. Hu, Y. Du, *Sci. Adv.* **2018**, *4*, eaau4511.
[40] M. L. Kiesel, C. Platt, R. Thomale, *Phys. Rev. Lett.* **2013**, *110*, 126405.

Manuscript received: January 5, 2024
Accepted manuscript online: February 5, 2024
Version of record online: February 28, 2024